

High-Resolution Bulgeless Liquid-Cell Electron Microscopy

Tyler S. Lott^{1†}, Ariel A. Petruk^{1†}, Nicolette A. Shaw¹, Natalie Hamada², Carmen M. Andrei²,
Yibo Liu³, Juewen Liu³ and Germán Sciaini^{1*}

¹The Ultrafast electron Imaging Laboratory (UeIL), Department of Chemistry and
Waterloo Institute for Nanotechnology (WIN), University of Waterloo, 200 University
Ave. W., N2L 3G1, Waterloo, Ontario, Canada

²The Canadian Centre for Electron Microscopy, McMaster University, A.N. Bourns
Science Building, 1280 Main St. W., L8S 4M1, Hamilton, Ontario, Canada

³Department of Chemistry and Waterloo Institute for Nanotechnology (WIN),
University of Waterloo, 200 University Ave. W., N2L 3G1, Waterloo, Ontario,
Canada.

†Equal contributions

*Correspondence: gsciaini@uwaterloo.ca

Abstract

Liquid cell electron microscopy (LCEM) has long suffered from irreproducibility and its inability to confer high-quality images over a wide field of view. LCEM demands the encapsulation of the *in-liquid* sample between two ultrathin membranes (windows). In the vacuum environment of the electron microscope, the windows bulge, drastically reducing the achievable resolution and the usable viewing region. Herein, we introduce a shape-engineered nanofluidic cell architecture and an air-free drop-casting sample loading technique, which combined, provide robust bulgeless imaging conditions. We demonstrate the capabilities of our approach through the study of *in-liquid* model samples and quantitative measurements of the liquid layer thickness. The presented LCEM method confers high throughput, lattice resolution across the complete viewing window, and sufficient contrast for the observation of *unstained* liposomes, paving the way to high-resolution movies of biospecimens in their near native environment.

Main

Liquid-cell electron microscopy (LCEM)¹⁻⁷ is a known state-of-the-art technique used to perform high-magnification imaging of nanomaterials and biological specimens which are suspended in a liquid inside of a nanofluidic cell (NFC). There are two types of LCEM systems; those connected to a syringe pump and capable of conferring liquid flow, commonly known as ‘flow LCEM systems’⁸⁻²⁴, and those which are stationary systems²⁵⁻⁴² herein referred to as ‘static LCEM systems’. Current LCEM technology is limited in its ability to precisely control the effective thickness of the liquid layer. In most commercially available silicon-based nanofabricated NFCs –those having silicon nitride (SiN_x) membranes as the window material– even a tiny droplet with a volume of 1 nL suffices for the liquid sample to overrun the spacer area. In addition, window bulging^{7,9,19-22} arises from the pressure differential experienced by the ultrathin window membranes when the NFC is inserted into the high vacuum environment of the electron microscope column for observation. Given that nanofluidic cells are typically assembled in the open laboratory environment, the internal pressure of the NFC assembly is unregulated and leads to variability in the effective liquid layer thickness, which depending on window size could be many times thicker than the nominal height of the predefined spacer. This effect is verifiable *via* different methods that can be applied to determine the thickness of the specimen *in situ*⁴³⁻⁴⁵. Moreover, standard NFCs are based on two ‘flat’ silicon chips with an imprinted spacer onto one of the dies. Thus, they are vulnerable to particle contamination from chip handling and the surrounding laboratory atmosphere, *vide infra*. The combination of all these detrimental effects cause irreproducibility and loss of resolution, usually limiting the usable viewing area to the corners of the windows^{21,24}. Window bulging is often more severe in the case of static NFCs, which lack an external control of the inner cell pressure, such as the liquid pumping station and/or

a vacuum line that may be attached to the outlet tube of a flow LCEM system^{8–10}. For this reason, many research groups have abandoned the use of conventional static SiN_x NFCs while others have developed approaches to reduce the liquid layer thickness, such as the implementation of slow evaporation²², the formation of gaseous voids and bubbles^{18,46–49}, and the use of patterned microwells^{38,39}. On the other hand, window fracture remains a concern during the operation of flow LCEM systems inside expensive TEMs because of their connections to a syringe with a large volume of liquid and the room atmosphere *via* the inlet and outlet tubes, respectively. Therefore, flow LCEM systems necessitate the use of a time-consuming leak-check station, and their NFCs usually have SiN_x membranes thicknesses in the range of $t_{SiN_x} \approx 30 \text{ nm} - 50 \text{ nm}$, with 50 nm being the most common in order to provide robustness at the expense of electron beam transparency⁵⁰. As a result, a large portion of the high-resolution LCEM work is nowadays relying on the encapsulation and formation of small pockets of liquid between two ultrathin membranes made of amorphous carbon^{51,52}, graphene^{29–37}, or their combination with SiN_x to produce hybrid NFCs^{40,41}. Among these choices, graphene cells (GCs)^{29–35,37} have become the standard to achieve atomic resolution in LCEM experiments. However, GCs are produced on a case-by-case basis, and handling graphene layers requires a great level of expertise and NFC engineering³⁷ to circumvent the high degree of variability of the liquid layer thickness caused by sample encapsulation⁴².

In this article we introduce a robust static LCEM method⁵³ that provides high-contrast and high-resolution images across the whole viewing area (*ViA*) with layer thicknesses ranging from ≈ 60 nm to 160 nm depending on the predefined nominal spacer's height (h_{nom}). The presented LCEM technology builds on the implementation of shape-engineered NFCs with $t_{SiN_x} \approx 20 - 30$ nm and

a fast and simple air-free drop-casting sample loading approach which confers bulge-free imaging conditions.

Improved Nanofluidic Cell Architecture

Figure 1 shows a comparison between a standard (flat) nanofabricated bottom NFC chip (Fig. 1a – c), our bottom NFC chip (Fig. 1d, e) and assembled cell (Fig. 1f). Note that the definition of ‘bottom’ and ‘top’ chips is arbitrary, and a standard top chip is completely flat and has no spacer. Figure 1a illustrates a tiny 2.5 nL droplet (at scale) positioned onto the window of a conventional 3 mm x 3 mm square NFC chip with a ≈ 1 mm wide nanochannel. Thus, if such a NFC die has a $h_{nom} = 200$ nm, any volume in excess of $1 \text{ mm} \times 3 \text{ mm} \times 200 \text{ nm} = 0.6 \text{ nL}$ will suffice for the liquid to invade the spacer area upon NFC assembly, and therefore lead to a thicker effective liquid layer. Therefore, one should deliver a volume of the order of 0.1 nL to try to avoid liquid overflow. Dispensing such a small amount of liquid, although possible, is not attainable through the use of commonly used micropipettes. Liquid overflow would also impact some flow LCEM systems that require the user to drop-cast the NFC before initiating the pumping of liquid to reduce the chances of membrane fracture.

Moreover, standard NFCs are also vulnerable to particle contamination, which may arise from chip handling as well as exposure to the laboratory atmosphere. NFC handling is typically conducted with a soft pair of tweezers as illustrated in Fig. 1b, and often results in microparticle contamination due to chip edge damage (Fig. 1c) and microparticle attraction caused by triboelectric forces⁵⁴. It should also be noted that a typical ISO Class 5 cleanroom contains up to 832 (size of $\geq 1 \mu\text{m}$) and 3520 (size of $\geq 0.5 \mu\text{m}$) airborne particulates per cubic metre⁵⁵, which are larger than the typical h_{nom} that ranges from 100 nm to 500 nm. Thus, the assembly of NFCs

should be carried out in an ISO Class 3 or better clean zone as a very first step toward trying to achieve some degree of reproducibility in LCEM experiments. HEPA filtered flow hoods can easily provide such a controlled environment⁵⁵.

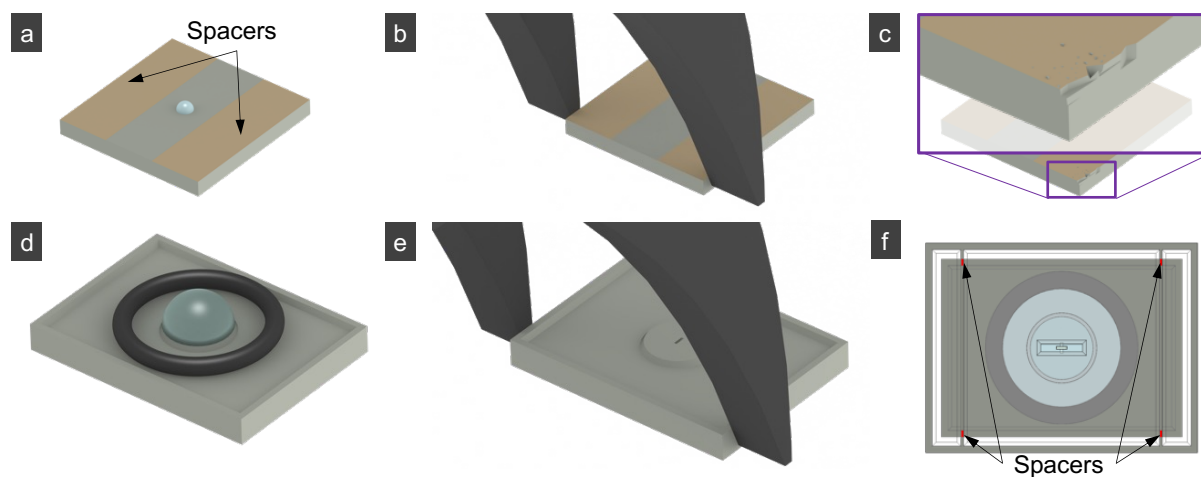


Figure 1: Comparing a conventional NFC to our recently developed NFC architecture. **a.** A standard or ‘flat’ NFC chip with a deposited spacer on the sides. The volume of the droplet illustrated here is 2.5 nL and resides on the window. As a scale reference, this chip has size of 3 mm x 3 mm. **b.** Handling of a conventional NFC with plastic tweezers. **c.** Handling leads to damage and microparticle contamination on the spacer region. Note that this has been exaggerated for illustrative purposes because usually these particles and the broken edge are not observable by the naked eye. **d.** Our recently developed NFC. The droplet volume indicated here is 500 nL; the typical volume we use to drop-cast our samples. **e.** Handling of the developed cell with plastic tweezers. **f.** An example of the recently developed NFC in assembly. The small red areas indicated by the black arrows highlight the regions of spacer overlap between the top and bottom nanofluidic chips. The surfaces defining the spacer’s height are far from those in contact with the tweezers.

Figure 1d displays our bottom NFC with a 500 nL droplet (at scale), which is the typical liquid volume we dispense *via* drop-casting onto its central pillar (**Supplementary Fig. S1a**). Moreover, in contrast with pioneering static NFC approaches that relied on capillary forces for liquid

loading^{25–28}, drop-casting is a general and more convenient approach for dispensing *in-liquid* specimens. Furthermore, the liquid droplet self-positions onto the *VIA* owing to the shape of the central pillar and the surface tension of the aqueous solution. Sealing is achieved through the implementation of an internal O-ring that encloses the liquid (Fig. 1f), circumventing the use of epoxy^{25,27}. This O-ring also forms a cavity around the central pillar that receives the excess of liquid upon NFC closure and serves as a protective barrier for the liquid not to reach the surfaces defining h_{nom} (highlighted in red in Fig. 1f). Furthermore, the bottom and top NFCs were engineered to assure that microparticle contamination caused by chip handling (Fig. 1e) does not impact the surfaces that define h_{nom} . In addition, h_{nom} is predefined and built-in during the nanofabrication process and can be varied within the range of 0 – 20 μm to accommodate for sample size (though resolution would decrease with the increase of t_w). The generation of top NFC chips implemented in this work had a rectangular-like central pillar as shown in Fig. 1f and Supplementary Fig. S1b; however, the actual shape of this feature is not essential to the performance of our method.

Our NFCs are produced *via* wafer-scale nanofabrication processes and their static design confers robust sealing through the implementation of a single internal O-ring and has been tested for weeks under ultrahigh vacuum conditions. It should be emphasized that the assembly of the NFC sandwich must be performed in a dedicated loading station and using a custom holder. The sample loading station confers an air-free environment. Any intention to close the NFC under the regular laboratory atmosphere would result in air being trapped inside the NFC cavity formed by the O-ring followed by a sudden increase of the internal pressure and the rupture of the window membranes.

Air-Free NFC Sealing Method for Drop-Casted Samples

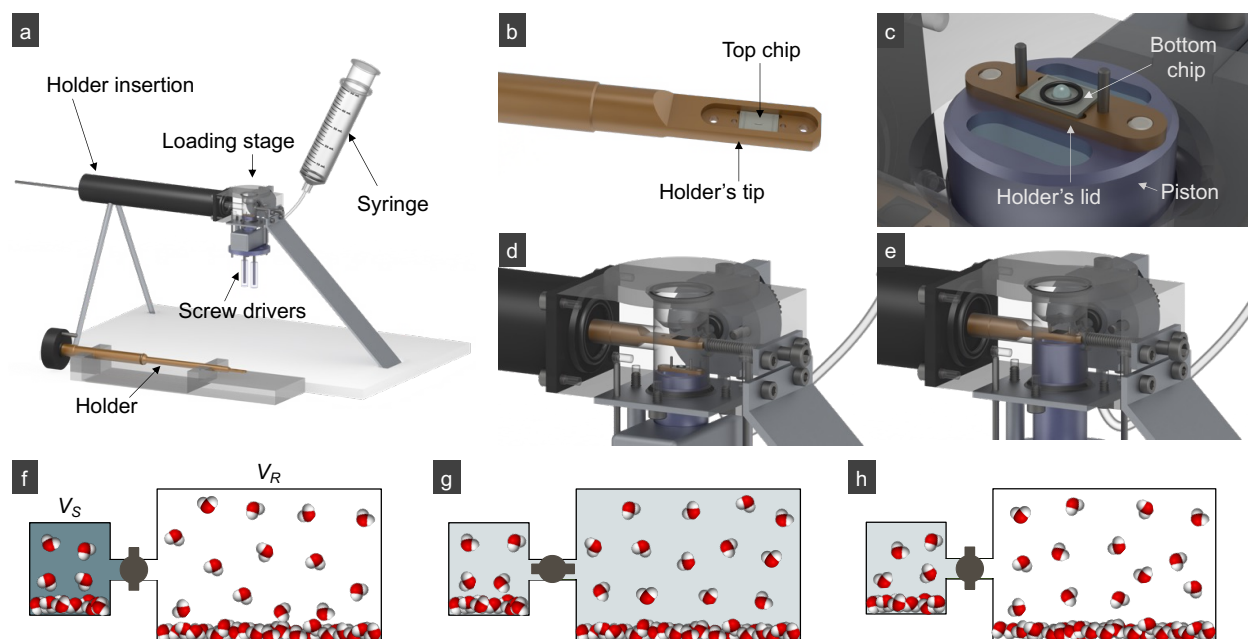


Figure 2: Loading NFCs in the absence of air – under a saturated solvent vapour atmosphere. a.

Complete LCEM kit for the study of drop-casted *in-liquid* specimens. The LCEM kit comprises a custom holder, an airtight sample loading stage and specially engineered NFCs, which are sealed in the absence of air. **b.** Holder's tip with the top NFC in position. **c.** Holder's lid and bottom NFC with the internal O-ring and dispensed sample are resting on a movable piston with alignment pins. **d.** Close view of the loading stage with the piston locked in position for air evacuation. **e.** Piston in position for the NFC chips to form a closed cell. The holder and piston are coloured for clarity. **f–h.** Illustration of the air evacuation process. Water molecules are represented with the space-filling model and air is represented by the dark and light grey backgrounds (the intensity of the colour correlates with air density). The dense water liquid phase is at the bottom of the containers with the gaseous phase located directly above. The container on the left with volume V_S represents the dead volume of the loading stage. The container on the right with volume V_R represents the volume of the syringe with its piston locked after forced expansion. **f.** At this moment the available volume in the syringe and loading stage are saturated in water vapour and $p_{air} \approx 100$ kPa in the loading stage and $p_{air} \approx 0$ in the syringe. **g.** The valve is opened for air to flow from the stage to the syringe until p_{air} in V_S and in V_R are equal. **h.** The valve is closed, the syringe is disconnected, evacuated, and reconnected, to repeat the process.

Figure 2 shows the complete LCEM kit, which comprises the holder and the loading station, illustrated in Fig. 2a, and the top and bottom NFC chips that are shown in Fig. 2b, c, respectively. Prior to sealing the NFC inside of the loading stage, the top NFC chip is placed into the holder's tip (Fig. 2b) and held in place from the outer back surface by a retainer with a small piece of carbon tape. The bottom NFC chip is placed onto the holder's lid which in-turn is positioned onto a movable piston with alignment pins (Fig. 2c). The liquid is drop-casted onto the central round pillar of the bottom NFC chip, and the piston is pulled down and locked in proper position to bring the bottom NFC chip inside the loading stage and introduce the cover lid of the loading stage, and the holder (Fig. 2d). At this moment, the loading stage is airtight, which is achieved through the implementation of O-rings placed between all key surfaces. An inverted syringe with a small amount of liquid is used to create a vapour saturated pseudo-vacuum environment upon volume expansion (V_R in Fig. 2f). After volume expansion, the syringe's piston is locked in place. It should be noted that at this point the vapour pressures (p_w) or chemical potentials (μ_w) of water – the solvent we employed in our LCEM experiments – in the loading stage and the syringe are the same. This step is critical and assures that there is only a net mass transfer of air (illustrated as a grey background) from the loading stage to the syringe when the valve is opened (Fig. 2f). Note that the loading stage's piston displayed in Fig. 2c has two pockets. These are also filled with liquid water to facilitate vapour saturation inside the loading stage. Once the air is transferred (after a minute or so), the valve is closed (Fig. 2g), the syringe is disconnected, evacuated by bringing its piston to the original position and refilling the tubing with water, and reconnected to repeat the same step; however, with already a lower partial pressure of air (p_{air}) inside the loading stage (Fig. 2h). It is straightforward to deduce, using the ideal gas equation, the following expression,

$$p_{air,f}(n) = p_{air,i} \left(\frac{V_S}{V_S + V_R} \right)^n$$

Where $p_{air,i}$ is the initial p_{air} and $p_{air,f}$ is the final p_{air} inside of the loading stage after the air evacuation process is repeated n times, V_S is the dead volume inside the loading stage, and V_R is the internal volume of the syringe. Ideally, if $V_R \gg V_S$ then $p_{air,f} \ll p_{air,i}$. There are practical limitations to the minimum attainable V_S and the maximum V_R (dictated by the size of the selected syringe). For our case, $V_S \approx 3$ mL and $V_R = 60$ mL, and $n = 3$. This results in $p_{air,f} \approx 0.013$ kPa, which is already $\ll p_w \approx 3.2$ kPa at room temperature, with p_w corresponding to the minimum achievable internal NFC pressure. Once the evacuation process is done, the valve is closed, the loading stage's piston is released, and the NFC is sealed, practically, in the absence of air. The implementation of pins provides a high degree of alignment and airtight screw drivers are used to secure the holder's lid and sealed NFC. After this final step ([Fig. 2e](#)) the syringe is removed, the loading stage is vented, its piston is pulled down, and the holder is taken out and ready for TEM imaging following the removal of the retainer. This method takes approximately 10 minutes to complete, i.e., to go from NFC assembly to imaging in the electron microscope. The leak check station that is usually implemented to test flow LCEM systems is no longer required owing to the very small volume of fully enclosed liquid ≈ 400 nL, which does not pose any risk to the electron microscope. [Supplementary Movie 1](#) illustrates the complete sample loading process.

Characterization of Membrane Bulging and Liquid Layer Thicknesses

We were able to measure, through the application of compressed gas and a contact profilometer, the maximum deformation (i.e., at centre of the membrane) for 25-nm thick SiN_x windows as a function of their width and the pressure differential (Δp) across the films; technical details about

our employed method can be found elsewhere⁹. For a $\approx 20\text{-}\mu\text{m}$ wide SiN_x membrane, we have determined a maximum deformation of $\approx 15\text{ nm}$ at $\Delta p \approx 3.2\text{ kPa}$ and $\approx 220\text{ nm}$ at $\Delta p \approx 100\text{ kPa}$ (see [Supplementary Note 3](#)). The former corresponds to the deformation anticipated when $\Delta p \approx p_w$; i.e., the minimum achievable value during TEM measurements. The latter represents the expected deformation when, for instance, a flow LCEM system with its outlet port open to the room atmosphere is used – a typical situation. We therefore expect at least a deformation of 440 nm ($= 220\text{ nm} \times 2$) in the centre of *ViA* when imaging with commercially available LCEM systems under flow conditions. The use of a high-quality inverted syringe, as shown in [Fig. 2](#), but connected to the outlet port of a flow LCEM system would largely mitigate this issue while air expansion against a ‘vapour-saturated vacuum’ would minimize the net transfer of solvent molecules and the chances of bubbling. Note that window bulging would still add to the aforementioned issues, i.e., particle contamination and liquid overrunning the spacer area, which lead to thicker effective liquid layers. Moreover, membrane deformation caused by pressurized gas can be considered as upper estimates because these measurements do not include the beneficial cohesive forces of liquid. Therefore, proper sealing of our NFC in the absence of air would result, for a $20\text{-}\mu\text{m}$ wide window, in a maximum deformation in the centre of *ViA* of 30 nm ($= 15\text{ nm} \times 2$), which is already acceptable to achieve high resolution.

To confirm that our LCEM technology actually confers negligible window bulging and determine the effective water layer thicknesses (t_w), we decided to carry out *in-situ* EELS measurements and apply the commonly employed log-intensity-ratio method introduced by Egerton and co-workers^{44,45} (see [Supplementary Note 4](#)). [Figure 3](#) exhibits the values of t_w calculated from EELS line scans for pure water when moving diagonally from one corner to the centre of the *ViA*. We performed a total of four independent measurements with NFCs having different h_{nom} . Results in

Fig. 3a involved the use of a Talos 200X operating at 200 kV while those in Fig. 3b were obtained at 300 kV in a Titan HB. In all four cases, we observed that t_w were below h_{nom} with a small amount of membrane deformation when $h_{nom} < 200$ nm and negligible bulging when $h_{nom} > 500$ nm. Although this observation was not expected at first, it can be explained by examining the sandwich structure shown in Fig. 3c, d. To ensure the contact between the surfaces highlighted in red in Fig. 1f, an external O-ring experiencing a higher compression and with a greater durometer was implemented. Following NFC closure, the compression of the O-ring leads to a net force that bows the bottom chip sufficiently to trap liquid between the windows if $h_{nom} < 200$ nm.

From the difference between t_w and h_{nom} in our measurements with $h_{nom} > 500$ nm we could estimate the maximum amount of chip bowing, which is approximately 440 nm – 480 nm. Some variations are anticipated due to the tolerances in the cross-sections of the O-rings. In addition, the water layer thickness of ≈ 40 nm observed at the edges of *ViA* when $h_{nom} < 200$ nm can be considered as the minimum achievable t_w limited by die-liquid-die compression. This value is expected to change depending on surface treatment. It is well-known that plasma cleaning increases the hydrophilic character of the SiN_x surface. We plasma cleaned the top chip's surface and kept the bottom chip's surface as produced. We found that this combination confers a desirable degree of hydrophilicity for the dispensed droplet to self-position onto the central pillar of bottom chip while providing high-resolution LCEM images across the complete *ViA*. Therefore, we decided to carry out all LCEM measurements, including EELS experiments, following this surface treatment protocol. Future group efforts will focus on performing the necessary modifications to achieve $t_w \approx h_{nom}$ to avoid the necessity to carry out EELS calibration measurements to determine the amount of die bowing.

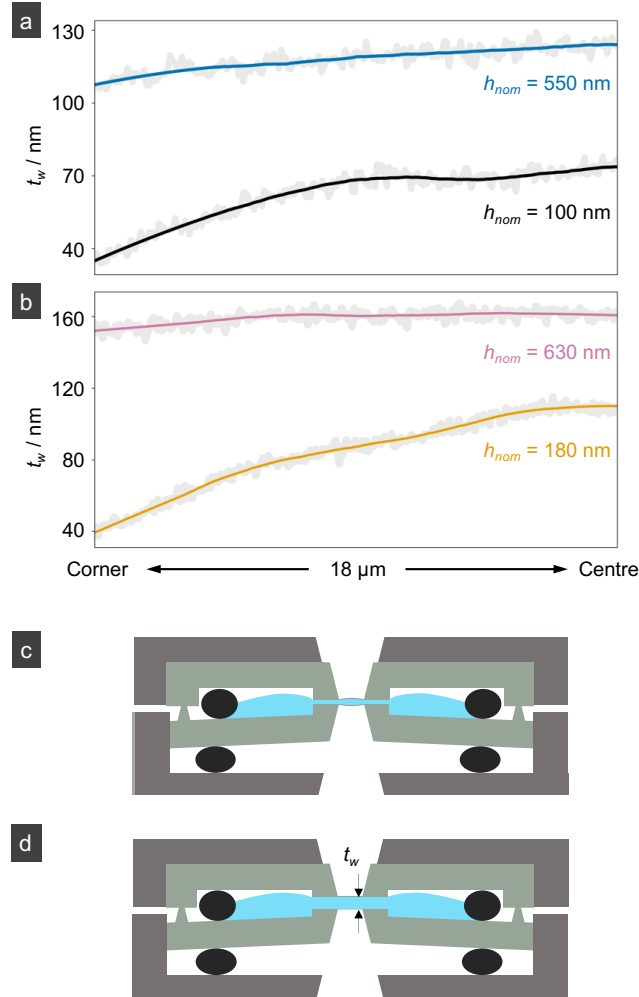


Figure 3: Liquid layer thickness measurements performed with pure water. **a, b.** EELS line-scan quantification of the water layer thickness (t_w) performed from the edge to the centre of the *Via* (see [Supplementary Fig. S4](#) for details) as a function of h_{nom} . Grey traces correspond to raw data. Coloured traces were obtained by smoothing the grey traces implementing a Savitzky-Golay filter. **a.** Experiments carried out in the Talos 200X at 200 kV for $h_{nom} = 100$ nm and 550 nm. **b.** Experiments carried out in the Titan HB at 300 kV for $h_{nom} = 180$ nm and 630 nm. **c, d.** Illustration of the cross-sectional view of assembled NFC in the holder's tip. The external O-ring (bottom black ellipses) has a higher durometer than the internal O-ring (top black ellipses) and is compressed to a larger extent to ensure the contact between the surfaces defining h_{nom} . Due to the difference in durometer and compression there is a net force that bows the bottom NFC chip and leads to $t_w < h_{nom}$. For small spacers, i.e., $h_{nom} < 200$ nm this die bowing

leads to liquid encapsulation and slight amount of membrane bulging (**c**). For $h_{nom} > 500$ nm bulging is negligible (**d**). Liquid layer thicknesses are in the range of $t_w \approx 60$ nm to 160 nm, which are ideal for high-resolution LCEM.

LCEM Studies of Model Systems

The following model samples were used to test the efficacy of our LCEM system: Citrate stabilized gold (Au) nanorods with a diameter of 15 nm and a length of 40 nm, polystyrene (PS) nanospheres with a diameter of 100 nm, and Dioleoyl-phosphatidylcholine (DOPC) liposomes. Au nanoparticles (NPs) are well known to give high-contrast images on account of Au's high atomic number, in addition the Au lattice is often utilized as a calibrant for high-resolution imaging. PS was implemented here as a model for a low atomic number material to illustrate that high-contrast images are possible in LCEM if the liquid layer thickness is comparable to the size of the particle. Lastly, unstained DOPC liposomes were imaged to demonstrate the potential for bioimaging. Samples were loaded as explained above and immediately taken to the electron microscope for imaging.

Images obtained with the Talos 200X at 200 kV near the edge and the centre of *ViA* using an NFC with $h_{nom} = 180$ nm are shown in [Fig. 4a](#) and [Fig. 4b](#), respectively. As expected, there is no evident degradation of image resolution, which is an indication of negligible bulging. We did observe, however, enhanced particle motion when moving from the edge ([Supplementary Movie 2](#)) to the centre of *ViA* ([Supplementary Movie 3](#)). This finding correlates with the slight increase of t_w caused by liquid encapsulation for $h_{nom} < 200$ nm, *vide supra*. Regardless the nominal spacer height that was in the range of $100 \text{ nm} \leq h_{nom} \leq 630$ nm, high-quality images were obtained in both TEM and high angle annular dark field scanning TEM (HAADF-STEM) modes. [Figure 4d](#), [e](#) show HAADF-STEM images recorded for Au NPs ($h_{nom} = 100$ nm) and PS NPs ($h_{nom} = 550$ nm),

respectively at 200 kV. [Figure 4f](#) shows a higher resolution TEM image of a Au NP obtained in the Titan HB at 300 kV near the *ViA*'s centre ([Supplementary Movie 4](#)). The line intensity profile shows a 20% – 80% change over only ≈ 0.9 nm. Given the cylindrical shape of the nanorod and the relative slow CCD camera implemented in this work (frame rate of 0.5s), 0.9 nm represents an upper limit of the spatial resolution. This observation confirms again that window bulging is indeed negligible. Over the course of many LCEM experiments on Au NPs, we have observed a variety of beam induced dynamics, such as nanoparticle-nanoparticle sintering, nanoparticle growth, and bubble formation (all available movies can be found in [Supplementary Information](#)).

Furthermore, [Fig. 4f](#) shows a TEM image obtained at 200 kV for unstained liposomes in aqueous solution. The quality of this image is remarkable for a specimen that would normally require the use of staining agents to be observed by LCEM with sufficient contrast^{56,57}. We observed electron beam induced sample damage progressing on a timescale of about a minute ([Supplementary Movie 7](#)), which provided us with sufficient time to record many images at a magnification of 22kx with a dose rate of $1.5 \text{ electrons } \text{\AA}^{-2} \text{ s}^{-1}$.

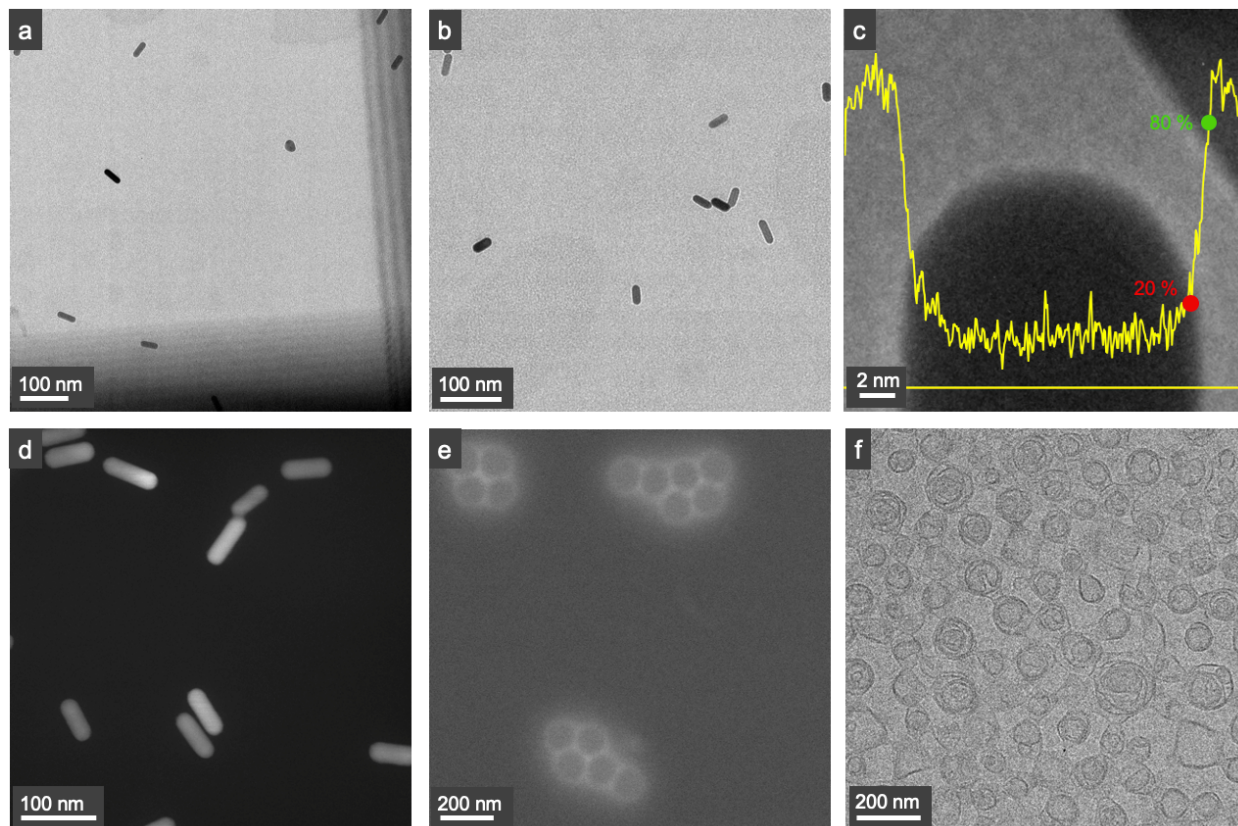


Figure 4: Characteristic LCEM images of model specimens. **a, b.** TEM (bright field) images of Au nanorods obtained near one corner (**a**) and near the centre (**b**) of the viewing area (*ViA*) in an NFC with $h_{nom} = 180$ nm. **c.** High-resolution TEM image of an Au nanorod in an NFC with $h_{nom} = 100$ nm. The yellow trace corresponds to the intensity profile along the yellow line crossing the NP and shows a 20%-80% intensity change in ≈ 0.9 nm. **d, e.** High angle annular dark field (HAADF) scanning transmission electron microscopy (STEM) images. **d.** Au nanorods in an NFC with $h_{nom} = 100$ nm. **e.** PS nanospheres in an NFC with $h_{nom} = 550$ nm. **f.** TEM image of unstained DOPC liposomes. All images with the exception of **a** were recorded near the centre of *ViA* of the NFCs. All images were obtained at 200kV with the exception of **c**, which was recorded at 300 kV. NFCs in these experiments had SiN_x windows with a thickness 30 nm (each) and a *ViA* $\approx 20 \mu\text{m} \times 20 \mu\text{m}$.

Figure 5 illustrates additional high-resolution images of a Au NP isolated from [Supplementary Movie 8](#), which was recorded under similar conditions to [Fig. 4c](#) and [Supplementary Movie 4](#), i.e.,

near the centre of *Via* at high resolution. This Au NP was found to remain relatively stationary, which is likely due to the enhanced interaction with one of the windows upon electron beam induced disruption of its stabilizing organic (citrate) capping layer¹². In this case and despite the limited capabilities of the employed CCD electron detector, we observed clear (2 0 0) and (1 1 1)-lattice planes with interplane distances of ≈ 0.20 nm and 0.23 nm, respectively ([Fig. 5b](#)). Planes were found to appear and disappear as the Au NP experiences slight changes of orientation with respect to the direction of the incident electron beam. Fourier and image analyses reveal that the central Au NP is composed of three single crystallites delineated with different colours in [Fig. 5a](#). This observation suggests that this Au NP was formed following electron beam induced particle-particle sintering and partial dissolution. The most noteworthy features in these TEM images are the small darker areas indicated by arrows. These correspond to Au nanoclusters/NPs with sizes ranging from ≈ 1 nm to 2 nm^{49,58}. For reference, the Au₁₃ cluster has a size of ≈ 0.85 nm⁴⁹. Therefore, our LCEM method allowed us to resolve small Au clusters. We then hypothesize that the beam-induced⁵⁹ areal growth rate of 25 nm² s⁻¹ of the Au NP observed towards the end of [Supplementary Movie 8](#) may arise via nanocluster⁵⁸ or particle coalescence⁴⁹. Note that Au nanoclusters freely experiencing Brownian motion in solution should not be observed with the implemented frame rate.

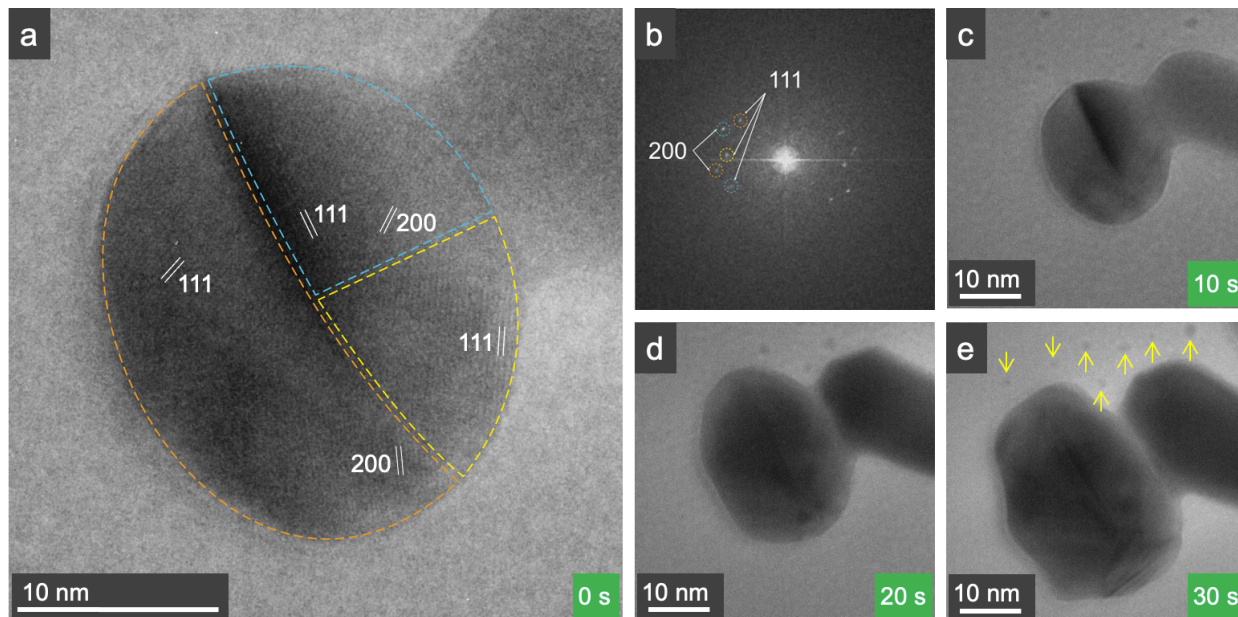


Figure 5: High-resolution LCEM imaging of Au NPs in solution. **a.** TEM image obtained in the Titan HB at 300 kV. Both (200) and (111) lattice planes were identified with interplane distances of 0.20 nm and 0.23 nm, respectively. The analysis reveals that this NP is comprised of three crystallites with the approximate interfaces delineated by dashed lines. This image was arbitrarily selected to define the time origin. **b.** A fast Fourier transform of the image shown in **a** with spots corresponding to (200) and (111) Au lattice planes. The colours correlate with each of the three crystallites in **a**. **c-e.** A sequence of TEM images of the same Au NP at later times showing growth. Small darker regions with sizes in the range of ≈ 1 nm – 2 nm are clearly identifiable and were indicated by yellow arrows in **e** to guide the eye. These regions correspond to small Au clusters. Time stamps in seconds are indicated on the bottom right corner of each image.

Conclusions

We presented a method which has solved window bulging – a long-lasting issue impacting the attainable resolution and field of view in LCEM. Our static NFC architecture and drop-casting loading approach are compatible for use with different types of membrane materials. Moreover, our air-free loading approach is broadly applicable and shows great promise in facilitating the assembly of other types of NFCs that are susceptible to air encapsulation. This key combination

provides reproducible high-resolution imaging conditions. Our results in the study of unstained liposomes are very promising and pose to drastically improve with 5-nm thick SiN_x windows that are currently in development. Note that in terms of electron beam transmittance⁵⁰, $t_{SiN_x} \approx 10$ nm corresponds approximately to $t_w \approx 40$ nm (Supplementary Note 5). Therefore, the difference in electron transmission relative to a GC can be, up to some degree, compensated by a slight reduction of the liquid layer thickness. Hence, we think that our LCEM technology will soon rival GCs by providing similar spatial resolution, higher throughput, and a much larger V_iA , traits which are essential for LCEM to advance the field of bioimaging.

Data availability

Full videos collected are available in the Supplementary Information. Raw datasets including metadata are available from the corresponding author upon reasonable request.

Code availability

Code used to perform liquid layer characterization (Supplementary Note 4), electron beam transmission estimation (Supplementary Note 5) are freely available to the public in GitHub repositories https://github.com/UeIL-Waterloo/EELS_analysis and https://github.com/UeIL-Waterloo/Electron_transmission.

Acknowledgements

We would like to acknowledge fruitful discussions with Tanya Prozorov (DOE Ames Laboratory, Iowa). We acknowledge financial support provided by the National Science and Engineering Research Council of Canada (NSERC), the Canada Foundation for Innovation (CFI), and the Ontario Early Researcher Award (ERA) program. This research was undertaken thanks in part to

funding from the Canada First Research Excellence Fund (CFREF). The University of Waterloo's QNFCF facility was used for the fabrication of NFCs. This infrastructure would not be possible without the significant contributions of CFREF-TQT, CFI, ISED, the Ontario Ministry of Research & Innovation, and Mike & Ophelia Lazaridis. LCEM experiments were performed at the Canadian Centre for Electron Microscopy (CCEM).

Contributions

G.S. conceived this research project. G.S. & A.A.P. invented this proprietary LCEM technology. T.S.L, A.A.P. & G.S. designed the LCEM holder and loading station. A.A.P., T.S.L. & N.A.S produced the NFCs at the University of Waterloo's QNFCF. T.S.L, A.A.P., N.A.S., G.S., N.H. & C.M.A. carried out the LCEM experiments at CCEM. Y.L. & J.L. synthesized the DOPC liposomes. T.S.L. and N.A.S. performed data analysis. T.S.L., N.A.S., A.A.P. and G.S. interpreted the results. G.S. and T.S.L. wrote the manuscript with helpful suggestions from all co-authors.

Competing interests

Sciaini, G. & Petruk, A. have submitted a patent application (US20220102110A1; Nanofluidic cell and loading platform) to the USA patent office.

References

1. Ross, F. M. *Liquid cell electron microscopy*. (Cambridge University Press, 2016).
2. De Jonge, N. & Ross, F. M. Electron microscopy of specimens in liquid. *Nat. Nanotechnol.* **6**, 695–704 (2011).
3. De Yoreo, J. J. & Sommerdijk. N. A. J. M. Investigating materials formation with liquid-phase and cryogenic TEM. *Nat. Rev. Mater.* **1**, 1–18 (2016).
4. de Jonge, N. *et al.* Resolution and aberration correction in liquid cell transmission electron microscopy. *Nat. Rev. Mater.* **4**, 61–78 (2019).
5. Pu, S., Gong, C. & Robertson, A. W. Liquid cell transmission electron microscopy and its applications. *R. Soc. Open Sci.* **7**, 191204 (2020).
6. Kelly, D. F. *et al.* Liquid-EM goes viral – visualizing structure and dynamics. *Curr. Opin. Struct. Biol.*

- 75, 102426 (2022).
7. Parent, L. R. *et al.* Tackling the challenges of dynamic experiments using liquid-cell transmission electron microscopy. *Acc. Chem. Res.* **51**, 3–11 (2018).
 8. Mueller, C., Harb, M., Dwyer, J. R. & Miller, R. J. D. Nanofluidic cells with controlled pathlength and liquid flow for rapid, high-resolution in situ imaging with electrons. *J. Phys. Chem. Lett.* **4**, 2339–2347 (2013).
 9. Petruk, A. A., Allen, C., Rivas, N., Pichugin, K. & Sciaini, G. High flow rate nanofluidics for *in-liquid* electron microscopy and diffraction. *Nanotechnology* **30**, 395703 (2019).
 10. Keskin, S., Kunas, P. & de Jonge, N. Liquid-phase electron microscopy with controllable liquid thickness. *Nano Lett.* **19**, 4608–4613 (2019).
 11. Woehl, T. J., Evans, J. E., Arslan, I., Ristenpart, W. D. & Browning, N. D. Direct in Situ Determination of the mechanisms controlling nanoparticle nucleation and growth. *ACS Nano* **6**, 8599–8610 (2012).
 12. Woehl, T. J. & Prozorov, T. The mechanisms for nanoparticle surface diffusion and chain self-assembly determined from real-time nanoscale kinetics in liquid. *J. Phys. Chem. C* **119**, 21261–21269 (2015).
 13. Bhattarai, N. & Prozorov, T. Direct observation of early stages of growth of multilayered dna-templated Au-Pd-Au core-shell nanoparticles in liquid phase. *Front. Bioeng. Biotechnol.* **7**, (2019).
 14. Proetto, M. T. *et al.* Dynamics of soft nanomaterials captured by transmission electron microscopy in liquid water. *J. Am. Chem. Soc.* **136**, 1162–1165 (2014).
 15. Evans, J. E., Jungjohann, K. L., Browning, N. D. & Arslan, I. Controlled Growth of Nanoparticles from Solution with In Situ Liquid Transmission Electron Microscopy. *Nano Lett.* **11**, 2809–2813 (2011).
 16. Patterson, J. P. *et al.* Observing the growth of metal–organic frameworks by in situ liquid cell transmission electron microscopy. *J. Am. Chem. Soc.* **137**, 7322–7328 (2015).
 17. Merkens, S. *et al.* Quantification of reagent mixing in liquid flow cells for Liquid Phase-TEM. *Ultramicroscopy* **245**, 113654 (2023).
 18. Serra-Maia, R. *et al.* Nanoscale chemical and structural analysis during in situ scanning/transmission electron microscopy in liquids. *ACS Nano* **15**, 10228–10240 (2021).
 19. Holtz, M. E., Yu, Y., Gao, J., Abruña, H. D. & Muller, D. A. In situ electron energy-loss spectroscopy in liquids. *Microsc. Microanal.* **19**, 1027–1035 (2013).
 20. Jungjohann, K. L., Bliznakov, S., Sutter, P. W., Stach, E. A. & Sutter, E. A. In situ liquid cell electron microscopy of the solution growth of Au–Pd core–shell nanostructures. *Nano Lett.* **13**, 2964–2970 (2013).
 21. Khelfa, A. *et al.* Quantitative in situ visualization of thermal effects on the formation of gold nanocrystals in solution. *Adv. Mater.* **33**, 2102514 (2021).
 22. Wu, H. *et al.* Mapping and controlling liquid layer thickness in liquid-phase (scanning) transmission electron microscopy. *Small Methods* **5**, 2001287 (2021).
 23. Grogan, J. M. & Bau, H. H. The nanoaquarium: a platform for in situ transmission electron microscopy in liquid media. *J. Microelectromechanical Syst.* **19**, 885–894 (2010).
 24. Ianiro, A. *et al.* Liquid–liquid phase separation during amphiphilic self-assembly. *Nat. Chem.* **11**, 320–328 (2019).

25. Williamson, M. J., Tromp, R. M., Vereecken, P. M., Hull, R. & Ross, F. M. Dynamic microscopy of nanoscale cluster growth at the solid–liquid interface. *Nat. Mater.* **2**, 532–536 (2003).
26. Zheng, H. *et al.* Observation of single colloidal platinum nanocrystal growth trajectories. *Science* **324**, 1309–1312 (2009).
27. Liao, H.-G., Cui, L., Whitlam, S. & Zheng, H. Real-time imaging of Pt₃Fe nanorod growth in solution. *Science* **336**, 1011–1014 (2012).
28. Liao, H.-G. *et al.* Facet development during platinum nanocube growth. *Science* **345**, 916–919 (2014).
29. Yuk, J. M. *et al.* High-resolution em of colloidal nanocrystal growth using graphene liquid cells. *Science* **336**, 61–64 (2012).
30. Park, J. *et al.* Direct observation of wet biological samples by graphene liquid cell transmission electron microscopy. *Nano Lett.* **15**, 4737–4744 (2015).
31. Ye, X. *et al.* Single-particle mapping of nonequilibrium nanocrystal transformations. *Science* **354**, 874–877 (2016).
32. Zhang, J. *et al.* Clean transfer of large graphene single crystals for high-intactness suspended membranes and liquid cells. *Adv. Mater.* **29**, 1700639 (2017).
33. Textor, M. & de Jonge, N. Strategies for preparing graphene liquid cells for transmission electron microscopy. *Nano Lett.* **18**, 3313–3321 (2018).
34. Clark, N. *et al.* Tracking single adatoms in liquid in a transmission electron microscope. *Nature* **609**, 942–947 (2022).
35. Wang, C., Qiao, Q., Shokuhfar, T. & Klie, R. F. High-resolution electron microscopy and spectroscopy of Ferritin in biocompatible graphene liquid cells and graphene sandwiches. *Adv. Mater.* **26**, 3410–3414 (2014).
36. Ghodsi, S. M., Megaridis, C. M., Shahbazian-Yassar, R. & Shokuhfar, T. Advances in graphene-based liquid cell electron microscopy: working principles, opportunities, and challenges. *Small Methods* **3**, 1900026 (2019).
37. Kelly, D. J. *et al.* Nanometer resolution elemental mapping in graphene-based TEM liquid cells. *Nano Lett.* **18**, 1168–1174 (2018).
38. Hutzler, A. *et al.* Unravelling the mechanisms of gold–silver core–shell nanostructure formation by in situ TEM using an advanced liquid cell design. *Nano Lett.* **18**, 7222–7229 (2018).
39. Pohlmann, E. S. *et al.* Real-time visualization of nanoparticles interacting with glioblastoma stem cells. *Nano Lett.* **15**, 2329–2335 (2015).
40. Dahmke, I. N. *et al.* Graphene liquid enclosure for single-molecule analysis of membrane proteins in whole cells using electron microscopy. *ACS Nano* **11**, 11108–11117 (2017).
41. Dearnaley, W. J. *et al.* Liquid-cell electron tomography of biological systems. *Nano Lett.* **19**, 6734–6741 (2019).
42. Keskin, S., Pawell, C. & de Jonge, N. Verification of water presence in graphene liquid cells. *Micron* **149**, 103109 (2021).
43. Langmore, J. P. & Smith, M. F. Quantitative energy-filtered electron microscopy of biological molecules in ice. *Ultramicroscopy* **46**, 349–373 (1992).
44. Malis, T., Cheng, S. C. & Egerton, R. F. EELS log-ratio technique for specimen-thickness measurement in the TEM. *J. Electron Microsc. Tech.* **8**, 193–200 (1988).

45. Egerton, R. F. *Electron Energy-Loss Spectroscopy in the Electron Microscope*. (Springer US, 2011).
46. Zhu, G. *et al.* Atomic resolution liquid-cell transmission electron microscopy investigations of the dynamics of nanoparticles in ultrathin liquids. *Chem. Commun.* **49**, 10944–10946 (2013).
47. Mirsaidov, U., Ohl, C.-D. & Matsudaira, P. A direct observation of nanometer-size void dynamics in an ultra-thin water film. *Soft Matter* **8**, 7108–7111 (2012).
48. Grogan, J. M., Schneider, N. M., Ross, F. M. & Bau, H. H. Bubble and pattern formation in liquid induced by an electron beam. *Nano Lett.* **14**, 359–364 (2014).
49. Jin, B., Wang, Y., Jin, C., De Yoreo, J. J. & Tang, R. Revealing Au₁₃ as elementary clusters during the early formation of Au nanocrystals. *J. Phys. Chem. Lett.* **12**, 5938–5943 (2021).
50. Dwyer, J. R. & Harb, M. Through a window, brightly: a review of selected nanofabricated thin-film platforms for spectroscopy, imaging, and detection. *Appl. Spectrosc.* **71**, 2051–2075 (2017).
51. Zhu, C. *et al.* In-situ liquid cell transmission electron microscopy investigation on oriented attachment of gold nanoparticles. *Nat. Commun.* **9**, 421 (2018).
52. Yan, C. *et al.* Facet-selective etching trajectories of individual semiconductor nanocrystals. *Sci. Adv.* **8**, eabq1700 (2022).
53. Sciaini, G. & Petruk, A. Nanofluidic cell and loading platform. US20220102110A1, publication 2022-03-31.
54. Wang, Z. L. & Wang, A. C. On the origin of contact-electrification. *Mater. Today* **30**, 34–51 (2019).
55. Ramstorp, M. *Introduction to contamination control and cleanroom technology*. (John Wiley & Sons, 2008).
56. Gnanasekaran, K. *et al.* In situ Ni²⁺ Stain for liposome imaging by liquid-cell transmission electron microscopy. *Nano Lett.* **20**, 4292–4297 (2020).
57. Piffoux, M. *et al.* Monitoring the dynamics of cell-derived extracellular vesicles at the nanoscale by liquid-cell transmission electron microscopy. *Nanoscale* **10**, 1234–1244 (2018).
58. Qiao, L. *et al.* Particle or cluster: on the atomic structure of the seeds used in gold nanoparticle synthesis. (2022) doi:10.26434/chemrxiv-2022-r18wr.
59. Woehl, T. J. & Abellan, P. Defining the radiation chemistry during liquid cell electron microscopy to enable visualization of nanomaterial growth and degradation dynamics. *J. Microsc.* **265**, 135–147 (2017).